International Journal of Electrochemical Science 19 (2024) 100841

Contents lists available at ScienceDirect

International Journal of Electrochemical Science

journal homepage: www.editorialmanager.com/ijoes

Magneto-electrochemical water splitting performance of graphene oxide/nickel aluminum-layered double hydroxide nanocomposites

Farzad Nasirpouri [a,*], Leila Jafari-Foruzin [a], Solmaz Komari-Alaei [a], Amirali Farmani [a], Sara Fazli-Shokouhi [a], Naeimeh Sadat Peighambardoust [b]

[a] Faculty of Materials Engineering, Sahand University of Technology, Tabriz 51335-1996, Iran
[b] Koç University Boron and Advanced Materials Applications and Research Center (KUBAM), Sariyer, Istanbul 34450, Turkey

ARTICLE INFO

Keywords:
Graphene oxide
Water oxidation
Layered double hydroxide
Magnetic field

ABSTRACT

Designing efficient, cheap catalysts for oxygen production is very important for water electrolysis and green hydrogen production. Here, synthesis and electrocatalytic performance of graphene oxide (GO)/nickel-aluminum layered double hydroxide (NiAl-LDH) composites were investigated for water-splitting applications. The composition, microstructure, and morphology of the nanocomposites were confirmed by X-ray diffraction (XRD), Fourier-transform infrared spectroscopy (FT-IR), and field emission scanning electron microscopy (FE-SEM), and their water oxidation performance was examined in 0.1 M potassium hydroxide solution in the presence and absence of magnetic field. The results show that optimized GO/NiAl-LDH nanocomposite (GO-1 %/NiAl-LDH) exhibits the lowest overpotential compared with other prepared nanocomposites. This performance demonstrates comparable electroactivity to well-developed electrocatalysts like the perovskite-based electrodes, it also shows an improved electrocatalytic activity compared to NiAl-LDHs due to the presence of graphene oxide in the composite. We interpreted this significant performance to improve electron transform and high active site at the synthesized GO/NiAl-LDH composites. The best electrocatalytic activity with an overpotential of 443 and 473 mV at the current density 10 $mA.cm^{-2}$ were evidenced for GO-1 %/NiAl-LDH nanocomposite in the presence and absence of external magnetic field, respectively. Furthermore, the tafel slope were reported about 54 and 162 $mV.dec^{-1}$ in the presence and absence of magnetic field, respectively. This improved water oxidation can be attributed to the magneto-hydrodynamic effect and the increased number of metal sites on LDHs under the magnetic field.

1. Introduction

Hydrogen is one of the ideal and clean energy carriers with the possibility of production by electrolytic and photocatalytic decomposition of water, namely water splitting [1–5]. This method is one of the most promising and practical processes for producing green hydrogen with high purity [6–9], which has attracted the attention of many scientists [10–12]. Electrocatalytic water decomposition typically occurs in a two-electrode system, consisting of a cathode and an anode seperated by apprpriate membranes, where reduction and oxidation reactions take place [13]. Suitable electrolytes are present to facilitate charge and ion transfer between the electrodes [14]. In the past, the oxygen production reaction was generally carried out using metal oxides such as RuO_2 and IrO_2 [15–17]. The low abundance and high cost of these compounds are the main drawbacks, posing significant challenges for industrial-scale water oxidation [18]. Thus, the discovery of cost-effective and abundant electrocatalysts is a challenge at water oxidation[19].

In general, in the electrolysis of water, the oxygen production reaction is the half-reaction that plays a prominent role in determining the overall electrolysis voltage [20]. The water oxidation reaction is more complicated than the water reduction reaction because of its electrochemistry, the formation of O-O bond is associated with the transfer of four electrons and four protons [21,22]. Therefore, this reaction on the anode needs more potential than the water reduction reaction and works according to the following Eqs. (1, 2) in the acidic and alkaline environments, as listed below [23,24]:

$$2H_2O \rightarrow 4H^+ + 4e + O_2 \quad (1)$$

* Corresponding author.
E-mail addresses: nasirpouri@sut.ac.ir, f_nasirpouri@yahoo.com (F. Nasirpouri).

https://doi.org/10.1016/j.ijoes.2024.100841
Received 27 June 2024; Received in revised form 12 October 2024; Accepted 12 October 2024
Available online 15 October 2024
1452-3981/© 2024 The Author(s). Published by Elsevier B.V. on behalf of ESG. This is an open access article under the CC BY-NC-ND license (http://creativecommons.org/licenses/by-nc-nd/4.0/).

$$4OH^- \rightarrow 2H_2O + 4e + O_2 \quad (2)$$

During the production of oxygen, the electrocatalysts used as electrodes play a vital role in creating O-O bonds, so metals with variable oxidation states can play a more effective role in the electrocatalytic oxidation of water [25].

Layered double hydroxides (LDHs) compounded with transition metals exhibit various structures, such as two-dimensional (2D) forms, nanoarrays, microspheres, and multidimensional self-standing formats. These compounds can be doped or decorated with carbon-based nanomaterials. The high versatility of these components results in efficient performance in energy conversion applications such as water splitting, supercapacitors, and more[26–28]. Due to the significant electrocatalytic activity of LDHs for water oxidation, researchers are working to exploit novel ways to increase their activity with further studies. One of the significant problems of LDHs in water oxidation is their poor conductivity. Carbon nanostructures such as graphene and carbon nanotubes with a large surface area and high electron transport are good candidates [29,30]. However, the pristine base of carbon materials does not present significant electrochemical activity, which has stimulated hybridizing them with other electroactive materials like LDHs. Thus, coupling LDH and carbon-based materials has been shown to increase the electrocatalytic activity in water oxidation. Gong *et al.* reported that NiFe-LDH, could exhibit higher electroactivity and stability in the oxygen evolution than commercial catalysts like iridium (Ir) as a precious metal when grown on CNTs. In 1 M KOH, the potential of the working electrode of NiFe-LDH/CNT was 1.48 V to provide 5 $mA.cm^{-2}$ current density [31]. Yin et al. synthesized NiCo-LDH coupled with GO-CNTs and used it as a hybrid electrocatalyst to investigate the oxygen evolution reaction. NiCo-LDH/GO-CNTs composite showed a low overpotential of 290 mV at 10 $mA.cm^{-1}$ current density. Its Tafel slope was reported at 66.8 $mVdec^{-1}$, demonstrating its super stability over pure NiCo-LDH and commercial RuO_2 in the alkaline media. This work reported the intimate electron interaction between LDH and GO-CNTs [32]. In another study, porous NiFe-LDH (PLDH) was grown on GO with perpendicular and parallel forms. PLDH/0.1 g GO with an overpotential 236 mV at 10 $mA.cm^{-2}$ and Tafel slope of 52 $mV.dec^{-1}$ shows its best oxygen evolution reaction. Therefore, this compound showed higher activity than commercial IrO_2 and pure LDH in the same condition [33]. Han *et al.* synthesized the GO on the iron-layered double hydroxide hybrid arrays (GO-NiFe LDH) using the one-step electrodeposition method. The GO-NiFe LDH requires a cell voltage of around 1.48 V to drive 10 $mA.cm^{-2}$ for the whole water splitting [34]. Furthermore, the RGO/NiFe-LDH was investigated as a highly durable electrocatalyst for oxygen evaluation reaction (OER) because of the small overpotential (~ 250 mV in 0.1 M KOH) based on the onset of catalytic current and stability [35]. Ma et al. examined the catalytic activity of oxygen evolution of $Ni_{2/3}Fe_{1/3}$-GO and $Ni_{2/3}Fe_{1/3}$-rGO. They found that $Ni_{2/3}Fe_{1/3}$-rGO exhibited higher activity than $Ni_{2/3}Fe_{1/3}$-GO in OER. The overpotential of the $Ni_{2/3}Fe_{1/3}$-GO and $Ni_{2/3}Fe_{1/3}$-GO at 1 M KOH were 0.21 V and 0.23 V, respectively [36]. Although the GO/NiAl-LDH nanocomposite has been prepared by many researchers, its application for water oxidation has not yet been explored [37–39].

Although high-performance electrodes can be used for water electrolysis, it has been reported that gas bubbles can accumulate on the electrode surface, blocking active sites and increasing the overpotential of both HER and OER. Therefore, alternative methods have been proposed to reduce the accumulation of bubbles on electrodes and the bubble-induced void fraction between them, in order to minimize bubble-related inefficiencies. These approaches will be introduced in order to achieve high efficiency and high rate of oxygen production. One potential method is to apply external magnetic fields during the water oxidation process. An external magnetic field can enhance water oxidation through indirect effects, such as Lorentz force-driven movement that improves mass transport, or by leveraging the magnetic properties of electrocatalysts [40]. Forced convection is induced by the Lorentz force, $f_L = j \times B$ where j represents the current density and B is the magnetic induction. The Lorentz force promotes bubble detachment from the electrode surface, thereby reducing the bubble coverage. The current generated by the Lorentz force is typically explained by the magnetohydrodynamic (MHD) effect [41].

The water oxidation behaviour of NiAl-LDH based electrocatalysts has been widely studied. Table 1S summarizes the electrocatalytic activity of different NiAl-LDH based electrocatalysts which were generally deposited on nickel foam substrates or composited with other transition metals and polymers.

Based on the literature presented above, we understand that NiAl-LDHs composited with carbon-based nanostructures such as graphene and its derivation have remarkable prospects for efficient water electrolysis. To our knowledge, the investigation of NiAl-LDH-based electrocatalysts deposited on stainless steel, a cost-effective and commercially viable substrate, has not yet been demonstrated. Therefore, in this work, in order to improve water oxidation, NiAl-LDH was modified using the optimized amount of graphene oxide (GO). The prepared nanocomposite improved the electrical transfer at GO/NiAl-LDH. Furthermore, we applied magnetic fields to enhance OER efficiency. GO/NiAl-LDH electrocatalysts improve the magneto-electrochemical water oxidation owing to the Lorentzian movement under an external magnetic field and active sites by the nanocomposite. An enhanced oxygen evolution reaction using NiAl-LDH decorated with graphene oxide is introduced here as a novel electrocatalyst for water oxidation under an external magnetic field.

2. Experimental

2.1. Materials

Natural graphite powder was used to synthesize graphene oxide. The sodium nitrate ($NaNO_3$- 6535), potassium permanganate ($KMnO_4$-105080), sulfuric acid (H_2SO_4, 98 %-100713), hydrogen peroxide (H_2O_2, 35 %), and ammonium persulfate (APS-1.01209) were purchased from Merck company. Hydrochloric acid (HCl-35.4 %) is from Royalex-H125. Sodium carbonate, nickel nitrate hexahydrate, and aluminum nitrate nonahydrate were obtained from Aldrich. Double-distilled water was used for the synthesis.

2.2. Electrochemical activity

Linear sweep voltammetry (LSV), Tafel plots and electrochemical impedance spectroscopy (EIS) were used to examine the electrocatalytic activity of the synthesized nanocomposites. The LSV was investigated at a scan rate of 5 $mV.s^{-1}$ in 0.1 M KOH. The curves were reported without compensated cell resistance (iR). The EIS curves were recorded at frequencies ranging from 100 kHz to 10 mHz using an AC amplitude of 10 mV at the open circuit potential (OCP). A platinum rod electrode, a stainless steel electrode coated with GO/NiAl-LDHs using the drop-casting technique, and a saturated calomel electrode (SCE) were used as the counter, working, and reference electrodes, respectively. The electrochemical water splitting (oxidation) of the synthesized nanocomposites was studied in a 0.1 M KOH solution.

The working electrode was prepared using stainless steel (316 L SS) as the substrate. Stainless steel was firstly cut into 1 × 1 cm^2 samples, then ground on sandpapers up to 5000 mesh, then washed with ethanol and distilled water (DI) to eliminate any residual contaminations. Then, 0.005 g of prepared nanocomposite was dispersed in 10 cc of water. Stainless steel substrates were coated with 100 μL of the prepared suspension using the drop-casting method.

The effect of the external magnetic field on water oxidation was studied using a homemade electromagnet that applied a homogeneous magnetic field. The magnetic flux density applied for all experiments was constant $\mu_o H = 0.2\ T$. The electrochemical cell was exposed to the external magnetic field. The magnetic field was applied perpendicular to the surface of the working electrode.

2.3. Preparation of graphene oxide (GO)

We used Hummer's method to produce GO nanosheets. 0.5 g of graphite and 0.25 g of $NaNO_3$ were dissolved in the 13 mL H_2SO_4 in the 500 mL round-bottom flask. Then, the mentioned flask was transferred into the ice bath and mixed for 1 h until the viscous solution was produced. The oxidation agents, like 1.5 g $KMnO_4$ and 4.5 g $(NH_4)_2S_2O_8$, were gradually added to the mixture in a 1:3 ratio. When the oxidants were added, the mixture's temperature was maintained below 20°C. Then, the ice bath was removed from under the flask. So, the reflux was set up for the flask under mixing conditions for 24 h. Subsequently, the deionized water with a 35 mL volume was slowly poured into the mixture. Then, the temperature of the flask was raised to 98 °C. In the next step, 5.5 mL of 35 % vol H_2O_2 was added to the mentioned solution by controlling the medium's temperature to avoid any risks because of exothermic reactions after adding it. Eliminating metal ions can be achieved by entering the 20 mL of 10 %vol HCl in the flask. Subsequently, the deionized water with a 30 mL volume was added to the mixture. The mixing process continued until the bubbles didn't show themselves clearly. Ultimately, 30 mL of deionized water was added to the mixture. The bubbles were removed by mixing procedure. Finally, the obtained mixture was washed off and centrifuged with deionized water. This procedure was performed until the pH reached 7. The obtained product was dried off in an oven at 60 ºC [42,43].

2.4. Synthesis of NiAl-LDH

Nickel nitrate hexahydrate 0.005 M (0.046 g) was added to 50 mL of deionized water in a flask. Then 0.005 M (0.094 g) aluminum nitrate nonahydrate was added to the above mixture. After achieving the reaction pH at 10 by adjusting with dropwise addition of sodium hydroxide solution, the resulting suspension was heated at 60°C for 24 h for high crystality [44]. Then, the obtained sample was washed off three times with deionized water and dried at 50°C for 24 h.

2.5. Synthesis of nanocomposite NiAl-LDH/GO

0.003 g of graphene oxide was added to a balloon containing 10 mL of deionized water. Then 0.005 M (0.046 g) of nickel (III) nitrate and 0.005 M (0.094 g) aluminum nitrate were added. Then, the reaction mixture was adjusted to pH = 10 with a sodium hydroxide solution and stirred at 60°C for 24 h. The precipitate obtained was centrifuged and dried at 50°C for 24 h. The produced sample was labeled as NiAl-LDH/GO-0.3 %. Other composite percentages, including NiAl-LDH/GO-0.5 %, NiAl-LDH/GO-1 %, NiAl-LDH/GO-3 %, and NiAl-LDH/GO-5 %, were produced using the same method, with only the amount of GO varied in the first stage. The amounts of GO used were 0.005 g, 0.01 g, 0.03 g, and 0.05 g for the respective compositions.

3. Results and discussions

3.1. X-ray diffraction

Fig. 1(a), (b), (c), (d), (e), (f), and (g) illustrate XRD patterns of GO, NiAl-LDH, GO-0.3 %/NiAl-LDH, GO-0.5 %/NiAl-LDH, GO-1 %/NiAl-LDH, GO-3 %/NiAl-LDH, and GO-5 %/NiAl-LDH. The GO synthesized using the Hummer's method showed an intense peak at 11.57° after oxidizing the surface of the graphite [45]. Oxidizing the surface of graphite layers increased the interplanar distance between carbon planes from 0.35 for graphite to 0.77 nm for graphene oxide. The distance between planes was calculated using the Bragg equation [17].

$$2dSin\Theta = n\lambda \quad (3)$$

Where $\lambda = 1.54$ Å and $n = 1$.

The NiAl-LDH exhibits specific Bragg peaks at 11.42°,23.7°, 34.4°, 39.8°, 61.9°, and 63.1°,which correspond to (003), (006), (012), (015), and (113) planes, respectively. These results were consistent with those reported previously [46,47]. The lattice spacing of NiAl-LDH at 11.42° for the (003) lattice plane was calculated to be 0.77 nm using the Bragg equation. These XRD patterns demonstrate the similar interaction of CO_3^{2-} between the NiAl LDH and the graphene grown on it.

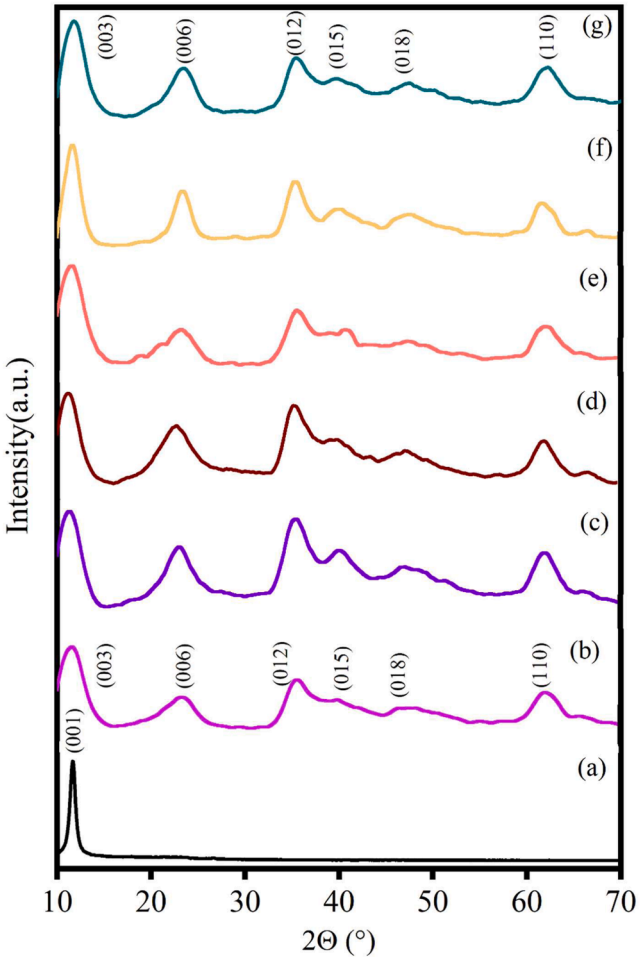

Fig. 1. XRD patterns of (a) GO, (b) NiAl-LDH, (c) GO-0.3 %/NiAl-LDH nanocomposite, (d) GO-0.5 %/NiAl-LDH nanocomposite, (e) GO-1 %/NiAl-LDH nanocomposite, (f) GO-3 %/NiAl-LDH nanocomposite, and (g) GO-5 %/NiAl-LDH nanocomposite.

Fig. 1(a) and (b) demonstrate that the GO and NiAl-LDH have distinct XRD patterns. It is evident that GO/NiAl-LDH-based composites with different compositions (0.3, 0.5, 1, 3, and 5 %) still retain the Bragg peak pattern of NiAl-LDH structure. However, the Bragg peak of GO at 11.57° overlaps with that of NiAl-LDH at 11.42°. On the other hands, as shown at Fig. 1(c-f), due to the low loading of graphene oxide, the peak of graphene oxide is not seen. Also, The other researchers reported that the diffraction peaks of carbon-based materials were weak or disappeared if the exfoliation destroyed the regular stacks of carbon-based materials [48,49].

By applying the Debye-Scherrer equation (Eq. (4)) [50] on the XRD patterns, the average crystallite size (D) of the GO, NiAl-LDH, and GO-NiAl-LDH nanocomposites can be calculated as:

$$D = \frac{0.9\lambda}{\beta \cos\theta} \quad (4)$$

where D is the crystallite size (in nm), "λ" is the wavelength of the X-ray used (in nm), "β" is the full width at half maximum (FWHM-in radian), and "θ" is the Bragg diffraction angle (in degree). The average crystallite

size, D, is calculated as: 9.2, 4. 7, 2.3, 2.4, 2.2, 3.0 and 2.3 nm for GO, NiAl-LDH, GO-0.3 %/NiAl-LDH nanocomposite, GO-0.5 %/NiAl-LDH nanocomposite, GO-1 %/NiAl-LDH nanocomposite, GO-3 %/NiAl-LDH nanocomposite, and GO-5 %/NiAl-LDH nanocomposite, respectively.

3.2. FT-IR spectra

Fig. 2 shows the FT-IR spectra of the NiAl-LDH, GO, and GO-1 %/NiAl-LDH. The FTIR spectrum of GO shows the characteristic peak at 3445.26 cm^{-1} corresponding to the OH groups. The peak correlated to the C═O demonstrated itself at 1724.59 cm^{-1} region [51,52]. The peak associated with the C═C bending is detected at 1590.98 cm^{-1} [52]. The absorption peak happened at 1388.90 and 1035.71, correlating to the C-O in the carboxylic (C-OOH) and epoxy (C-O), respectively [53]. Furthermore, the absorption at 874.78 cm^{-1} relates to the C-H, Fig. 2 **(a)**.

For NiAl-LDH, the FT-IR peak at 3400 cm^{-1} corresponds to the hydroxyl groups in NiAl-LDH and interlayer water molecules. The bending vibration of water molecules for NiAl-LDH structure can be detectable at 1632 cm^{-1}. Two absorption peaks at 1356 and 1382 cm^{-1} are related to the presence of carbonate ions with stretching vibrations of C═O and C-O functional groups, respectively [54]. The peaks at 608 and 835 cm^{-1} correspond to the existence of the hydroxyl and metal vibrations like the M-OH bond. The metal-oxygen (O-M-O) peaks can be detected at 438 cm^{-1} [55].

The FT-IR spectrum of GO-1 %/NiAl-LDH shows a peak at 3446 cm^{-1} corresponding to the stretching vibrations of hydroxyl groups. The peak at 1359 cm^{-1} is related to the stretching vibration of C═O because of the presence of carbonate anions. The M-O peaks appear at 830, 568, and 432 cm^{-1}.

3.3. Raman spectra

As shown in Fig. 3**(a)**, the Raman spectrum of GO shows two broad bands at 1395 (D) and 1595 cm^{-1}(G), which were attributed to the disordered graphitic lattices provided by sp^2 -sp^3 bonds in the GO sample and the in-plane vibration of sp^2 carbon atoms indicative of the formation of ordered graphene layers, respectively [56,57]. Typically, the ID/IG ratio is used to study the stacking order of graphene layers. A larger ID/IG ratio indicates a lower degree of graphitization. It can be estimated from the spectra that the ID/IG value is 1.02. It is noted that

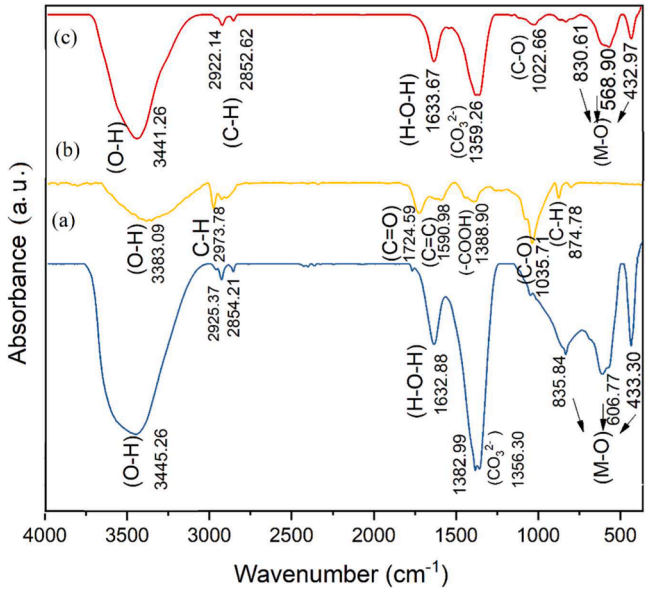

Fig. 2. FT-IR spectra of (a) NiAl-LDH particles, (b) GO particles, and (c) GO-1 %/NiAl-LDH nanocomposite.

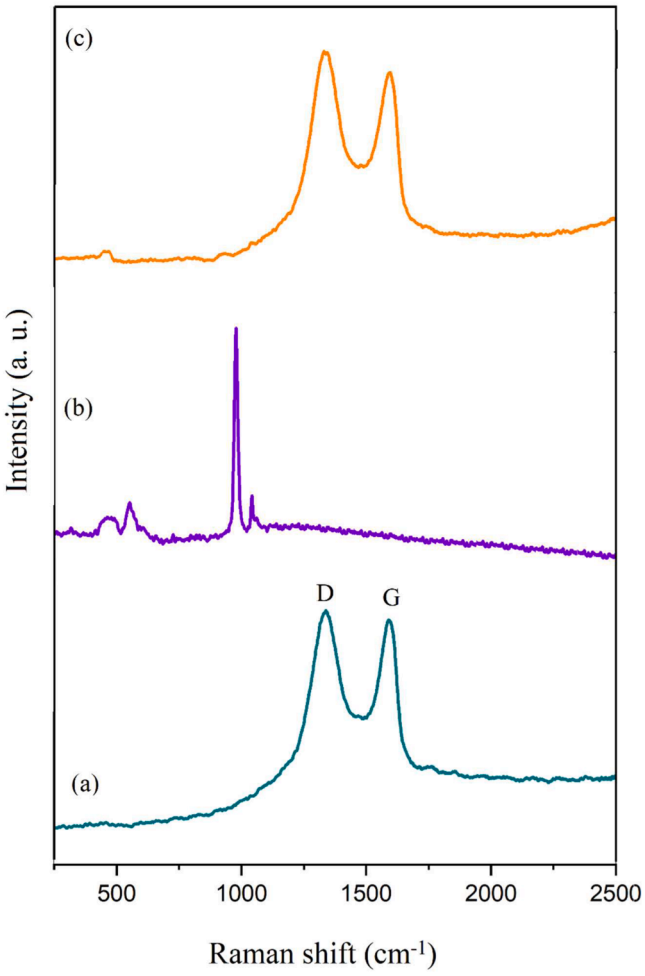

Fig. 3. Raman spectroscopy of (a) GO, (b) NiAl-LDH, and (c) GO-1 %/NiAl-LDH nanocomposite.

the prepared GO shows the lowest degree of graphitization, that is, more defects or structural disorders [58]. According to Fig. 3**(b)** for NiAl-LDH, the two peaks which were attributed to vibrations of Al^{3+}–O–Al^{3+} and Al^{3+}/Ni^{2+}–O–Ni^{2+} were have appeared at 483 and 551 cm^{-1}. Also, the peak at about 998 and 1043 cm^{-1} may originate from the symmetric stretching mode of interlayer carbonate at NiAl-LDH [59]. As shown in Fig. 3**(c)**, in the GO-1 %/NiAl-LDH nanocomposite, three peaks at 483, 998, and 1043 cm^{-1} correspond to NiAl-LDH in the composite. Also, the peaks that were shown at 1395 and 1595 cm^{-1} were attributed to GO. The intensity of the NiAl-LDH peaks in the nanocomposite increased compared to pure NiAl-LDH. This can be attributed to a decrease in crystallinity in the nanocomposite.

3.4. Morphology of GO/NiAl-LDH composites

FE-SEM images of NiAl-LDH and prepared GO/NiAl-LDH nanocomposites are shown in Fig. 4**(a-e)** which shows the morphology of the prepared composites. NiAl-LDHs are sheet-like and have a uniform structure, Fig. 4**(a)**. As presented in Fig. 4**(b)**, when the amount of composited GO was about 0.3 %, the size of nanoparticles was about 13 nm, however, it seems to assume aggregation between particles. For the nanocomposites with 0.5 % GO, the aggregation was decreased, and the size of nanoparticles increased to about 17 nm (Fig. 4**(c)**). For 1 % GO nanocomposites, the size of nanoparticles is about 20 nm, and aggregation was not remarkable (Fig. 4**(d)**). With increasing GO to 3 %, the size of nanoparticles was increased to 23 nm, but aggregation still happened (Fig. 4**(e)**). Furthermore, as shown in Fig. 4**(f)**, with

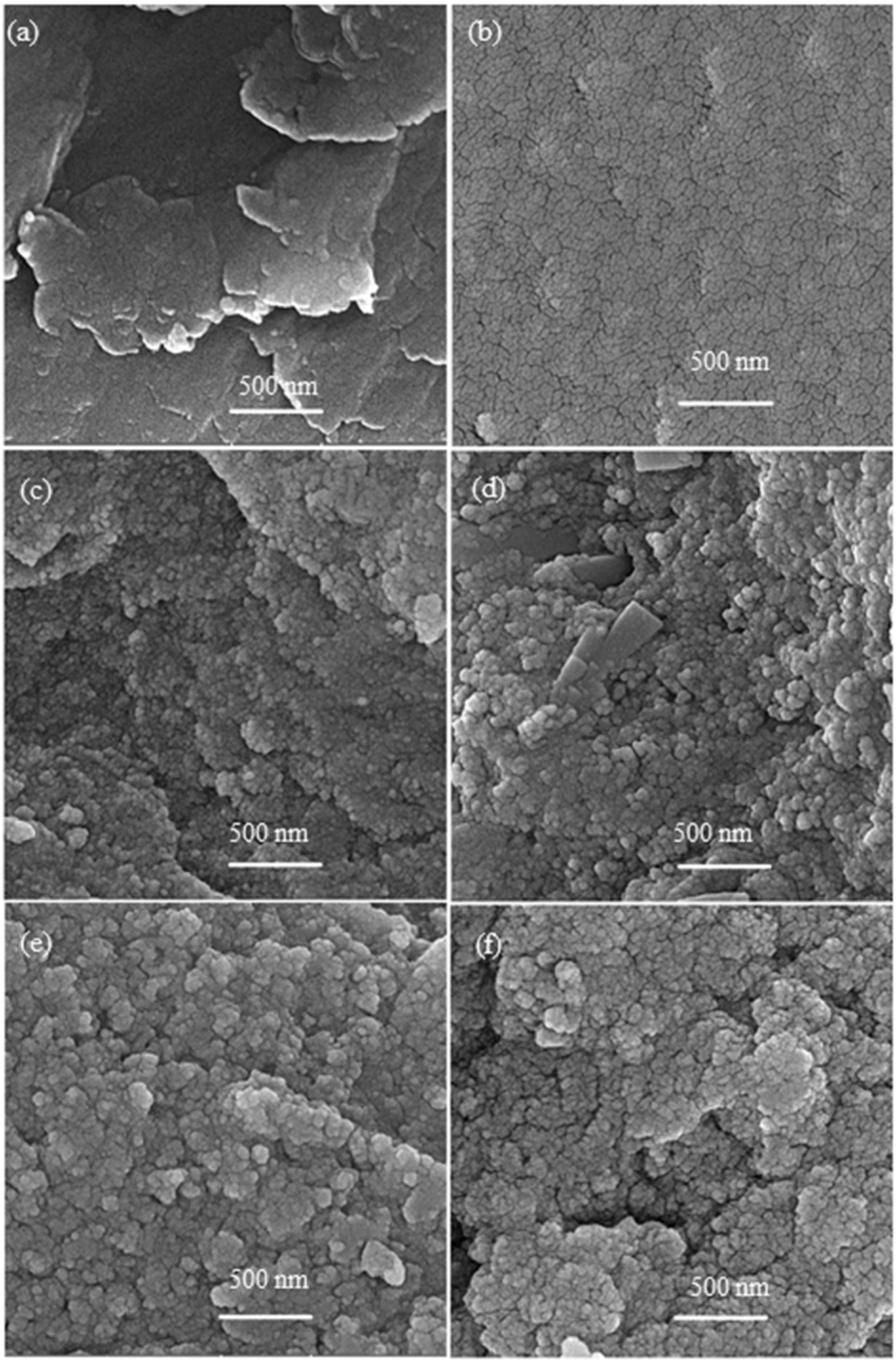

Fig. 4. FE-SEM images from (a) NiAl-LDH (b) GO-0.3 %/NiAl-LDH nanocomposite, (c) GO-0.5 %/NiAl-LDH nanocomposite, (d) GO-1 %/NiAl-LDH nanocomposite, (e) GO-3 %/NiAl-LDH nanocomposite, and (f) GO-5 %/NiAl-LDH nanocomposite drop casted on the stainless steel substrate.

increasing GO to 5 %, the size of nanoparticles was about 26 nm, but the aggregation still increased. Therefore, we understand that the optimized size without the aggregation, is evident for the nanocomposite GO-1 %/NiAl-LDH.

3.5. XPS analysis

XPS was employed to gain deeper insights into the surface chemistry and oxidation states of the samples prepared. Fig. 5 displays the high-resolution XPS spectra of GO, NiAl-LDH, and GO-1 %/NiAl-LDH. In Fig. 5**(a)**, the C 1 s spectrum of GO reveals three primary peaks at 284.50, 286.60, and 288.19 eV, corresponding to C-C, C-O (in hydroxyl groups), and C═O (in carbonyl groups), respectively. In the high-resolution O1s XPS spectrum, two distinct sub-bands are observed at binding energies (BE) approximately at 530.97 and 532.40 eV, attributed to the C═O and C-O functional groups, respectively.

Fig. 5**(b)** and **(c)** illustrate the C 1 s, O 1 s, Ni 2p, and Al 2p spectra for both NiAl-LDH and the GO-1 %/NiAl-LDH composite. In the high-

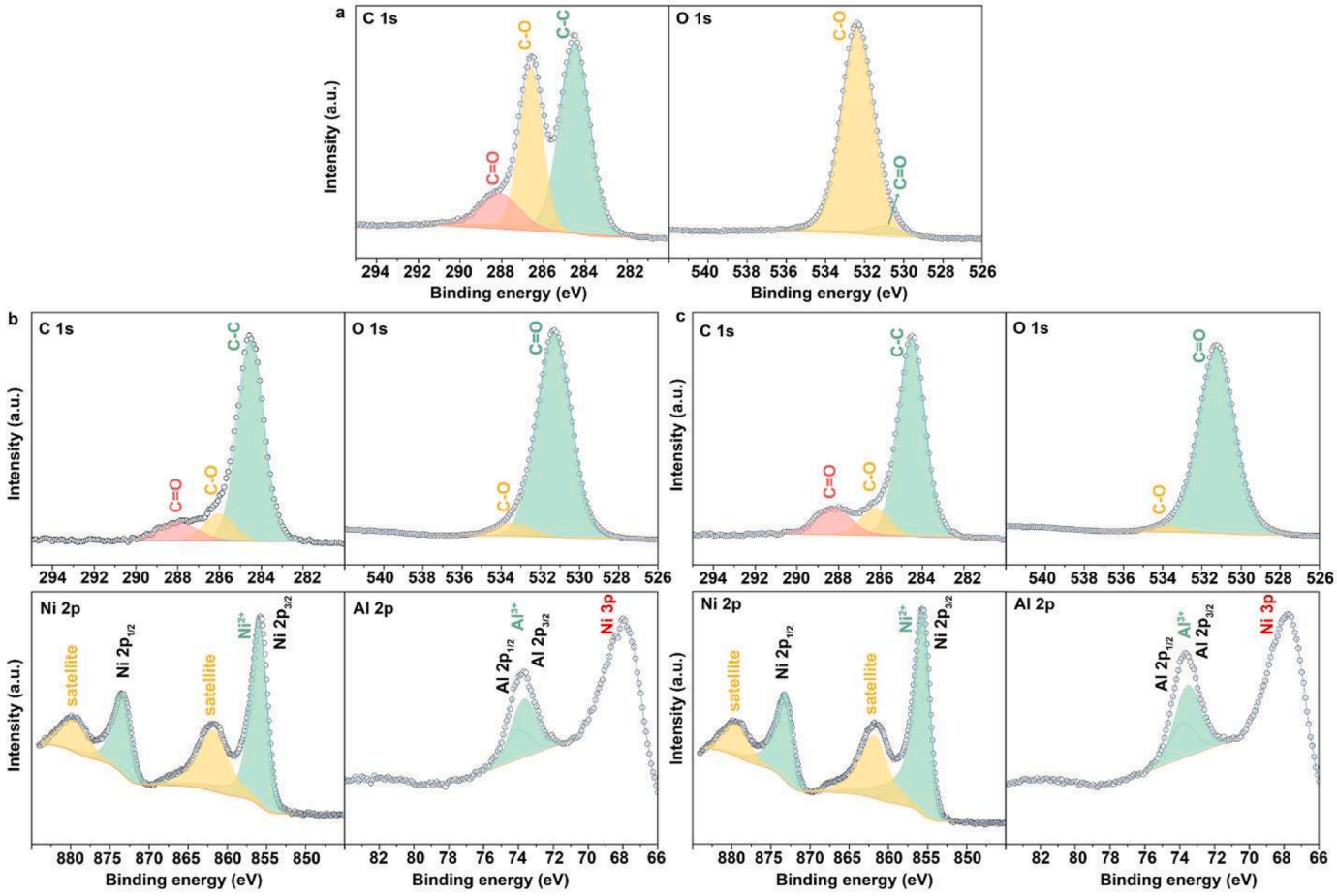

Fig. 5. High-resolution XPS spectra of C 1 s, O 1 s, Ni 2p, and Al 2p for a) GO particles, b) NiAl-LDH particles, and c) GO-1 %/NiAl-LDH nanocomposite.

resolution spectra of C 1 s within the GO-1 %/NiAl-LDH composite, the three regions around 284.50, 286.35, and 288.29 eV can be attributed to non-oxygenated ring C (C-C), C-O, and C═O species, respectively[60]. Similarly, the C 1 s spectrum of NiAl-LDH microspheres comprises three components, where one peak at 284.50 eV arises from incidental hydrocarbons. The other two, approximately at 285.93 and 287.91 eV, correspond to the C-O and C═O groups stemming from carbonate ions intercalated within the LDH interlayers. Notably, the BE of C-O and C═O in NiAl-LDH shifted from 285.93 eV and 287.9 eV to 286.35 eV and 288.29 eV after hybridization with GO. Furthermore, the atomic percentage of C═O increases from 3.7 % to 4.15 %, indicating a heightened presence of this group post-interaction between GO and NiAl-LDH. These shifts in BE and the increased atomic percentage of C═O suggest electronic interactions between NiAl-LDH and GO. The observed changes in binding energies indicate alterations in the electronic environment surrounding these functional groups, likely due to the formation of new chemical bonds or charge transfer interactions between the GO and the NiAl-LDH layers. Additionally, the NiAl-LDH exhibits two doublets in the Ni 2p region. The initial doublet at 855.98 and 873.43 eV corresponds to the Ni 2p3/2 and Ni 2p1/2 core levels, while the subsequent peaks at 861.80 and 879.55 eV represent their respective satellites, indicating the presence of nickel in a divalent form within NiAl-LDH[61]. The doublet at 73.66 and 73.98 eV pertains to Al 2p3/2 and Al 2p1/2 orbitals, signifying the formation of Al–OH [62].

Moreover, in the GO/NiAl-LDH composite, the BEs for the Ni 2p and Al 2p regions experience a slight negative shift in comparison to those of pure NiAl-LDH (from 855.89 to 855.62 eV in Ni 2p and from 73.66 to 73.46 eV in the Al 2p spectrum). This negative BE shift suggests a higher electron density within the LDH component. Considering the interaction between positively charged LDHs and negatively charged functional groups on GO nanosheets [63], this shift could indicate an electron transfer from GO to the LDH, causing the observed negative shift in the binding energies as a result of this electron transfer.

3.6. *Electrochemical water oxidation of GO/NiAl-LDH nanocomposites*

To investigate the electrochemical activities of the synthesized nanocomposites during water oxidation reactions, LSV curves were recorded in 0.1 M potassium hydroxide electrolyte solution. To compare the electrocatalytic activity of prepared materials, LSV curves of NiAl-LDH, GO and their nanocomposites with different compositions were studied in the presence and absence of the magnetic field, Fig. 6**(a)** and **(b)**.

According to LSVs of Fig. 6**(a),** the onset-potentials of water oxidation reaction for GO-0.3 %/NiAl-LDH, GO-0.5 %/NiAl-LDH, GO-1 %/NiAl-LDH, GO-3 %/NiAl-LDH, and GO-5 %/NiAl-LDH have been measured and compared with that of NiAl-LDH and GO. Based on Fig. 6 **(a)**, the GO cannot be active for water oxidation. The onset-potential of water oxidation for NiAl-LDH and GO was reported at about 0.66 and 0.73 V(vs. SCE), respectively. Among the prepared nanocomposites, GO-1 %/NiAl-LDH has the lowest onset potential for starting the water oxidation reaction, at 0.64 V vs. SCE.

We understand that the electrical conductivity of GO is higher than pure NiAl-LDH which has influenced positively the electrocatalytic activity of LDHs due to the large surface area and high speed of electron transfer. Among the nanocomposites synthesized with different GO content, it is evident that with an increase in the GO content to more

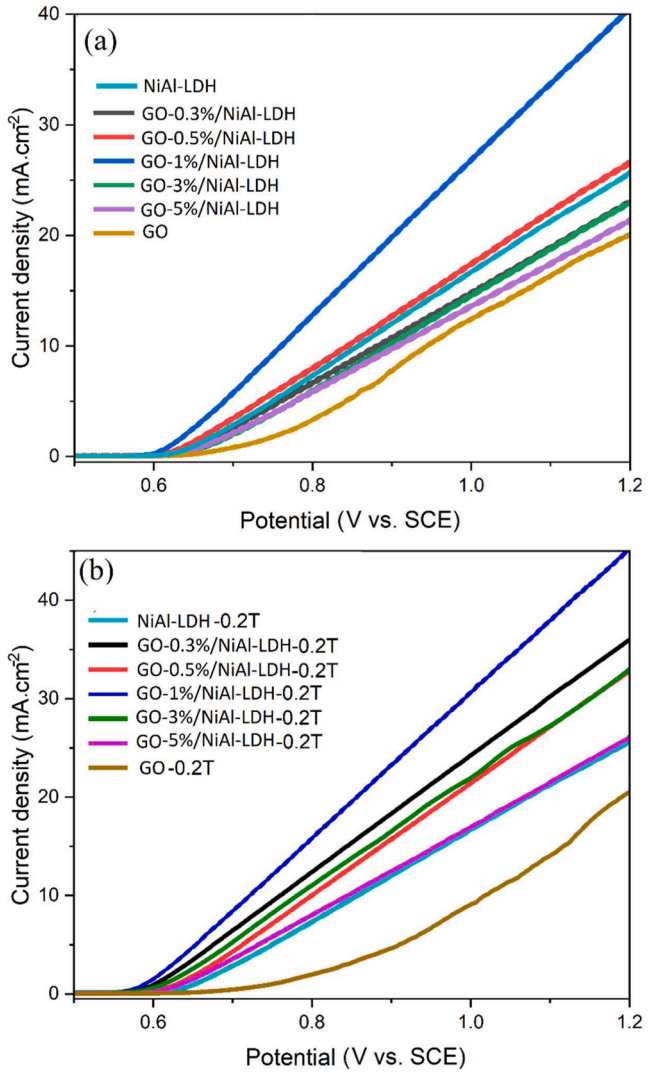

Fig. 6. LSV curves of GO particles, NiAl-LDH particles and GO/NiAl-LDH nanocomposites with different GO contents drop casted on stainless steel substrate at (a) absence magnetic field and (b) present magnetic field ($\mu_o H$=*0.2 T*).

than 1 %, the onset potential for water oxidation reaction decreased because the active sites of metals were decreased. Besides, pure GO does not have significant catalytic activity. However, for GO content less than 1 %, the water oxidation was not significantly improved owing to the decreased electrical conductivity of LDH. Since our results are consistent with those of Parida et al. [64], on GO/NiFe-LDH composites for water oxidation, the presence of an optimal amount of GO enhances the electrocatalytic activity of layered double hydroxides. It is worth noting that the best water oxidation performance achieved here is related to 1 % GO nanocomposite.

Fig. 6**(b)** presents the effect of a magnetic field on prepared nanocomposites. As shown in Fig. 6**(b),** there is a negligible effect on the water oxidation activity of GO, GO-0.3 %/NiAl-LDH and GO-0.5 %/NiAl-LDH under the magnetic field. However, the magnetic field improves the electroactivity of NiAl-LDH and the GO/NiAl-LDH with higher GO content. It is evident that under the influence of a magnetic field, the formation of oxygen bubbles on the LDH electrode decreases, which in turn enhances water oxidation. On the other hand, as the amount of GO increases, the number of active metal sites in the NiAl-LDH nanocomposite decreases, reducing the effect of the magnetic field. This can be attributed to the superior effect of GO enhancing the water splitting already attained for the GO/NiAl-LDH composites. For our optimal composite, GO-1 %/NiAl-LDH, the magnetic field has a greater impact compared to the other synthesized nanocomposites. The current density of GO-1 %/NiAl-LDH at 0.2 T was reported to be around 45 mA.cm^{-2}, which is higher than the current density of GO-1 %/NiAl-LDH without the magnetic field (40 mA.cm^{-2}).

Also, the onset potential of GO-1 %/NiAl-LDH 0.2 T for water oxidation was about 0.61 V(vs. SCE). The onset potential, and overpotential at current density 10 mA.cm^{-2} (η_{10}) for prepared nanocomposites under present and absent magnetic fields are compared and reported in Table 1 **and** Fig. 7**(a-c)**. The lowest onset potential was reported for GO-1 %/NiAl-LDH 0.2 T. This improvement can be attributed to the increased number of active sites and enhanced charge transfer, resulting from the optimized amount of GO and the beneficial effect of the magnetic field. The magnetic field, with its high metallic content and Lorentzian movement, repelled bubbles formed on the surface of the GO-1 %/NiAl-LDH electrode, thereby enhancing water oxidation.

We investigated the kinetics of the water oxidation reaction using the Tafel plots. Fig. 8**(a) and (b)** show the Tafel curves for prepared nanocomposites, GO and NiAl-LDH in KOH 0.1 M in the absence and presence of magnetic field. Accordingly, in the absence of a magnetic field, the GO-1 %/NiAl-LDH nanocomposite exhibits a Tafel slope of approximately 162 mV.dec^{-1}. Based on this Tafel slope, it can be inferred that water oxidation occurs via the Volmer–Heyrovsky pathway. [65]. This Tafel slope is lower than that of GO, NiAl-LDH and other prepared nanocomposites. Furthermore, under the effect of the magnetic field, the Tafel slope is reduced to 54 mV. dec^{-1}, which was the lowest Tafel slope amongst others. The reduced Tafel slope of GO-1 %/NiAl-LDH, both in the absence and presence of the magnetic field, can be attributed to a change in the water oxidation mechanism under the influence of the magnetic field.

We further examined the kinetic processes of the water oxidation on GO/NiAl-LDHs electrodes using EIS and exploited the electron transfer and/or mass transport dynamics at the interface between the electrode and electrolyte. Results are shown in Fig. 9**(a) and (b)**. The electrical equivalent circuits represent every element that can be observed in Fig. 9**(c)**. The parameters can be described as follows: R_s represents the resistance of the solution, R_{ct} signifies the charge transfer resistance associated with the reaction taking place at the working electrode, C_{dl} represents a capacitance linked to the double-layer capacitance of the working electrode, indicating the dispersion effect. R_p stands for the mass transfer resistance of the adsorbed intermediate H_{ads}, often referred to as pseudo-resistance[66].

In a typical EIS Nyquist plot, a reduction in the size of the circle represents an increase in charge transfer resistance at the electrode/electrolyte interface, indicating an improved electron transfer rate. Larger circle radii, on the other hand, suggest higher charge transfer resistance of the electrode system. According to Fig. 9(a), the presence of GO in all nanocomposites reduces both charge transfer resistance and mass transfer resistance. The increase of GO content results in a reduction in the mass transfer resistance. This reduction can be attributed to the electrical conductivity of GO and the formation of a conductive particle chain within the composite [67]. As we know, one of the main problems of LDHs is their low electrical conductivity and high charge transfer resistance. Therefore, the incorporation of GO into LDHs, solves this problem and improves catalytic properties by forming this conductive chain in the electrode[68]. The EIS results show that the charge transfer resistance (R_{ct}) of GO-1 %/NiAl-LDH is notably lower than that of pure GO and LDH and other composites, suggesting more effective integration of GO-1 %/NiAl-LDH nanocomposites during charge transfer. Consequently, the electrical conductivity is enhanced. Additionally, the reduction in charge transfer resistance in the GO-1 %/NiAl-LDH composite, resulting from improved synergy, has led to a significant increase in double-layer capacitance. This implies that GO-1 %/NiAl-LDH nanocomposites exhibit higher capacitance and catalytic properties than pure GO, NiAl-LDH and their nanocomposites. This evidence is supported by the EIS data, which reveals a reduced

Table 1
Onset potential, and overpotential at current density 10 mA.cm^{-2} (η_{10}) for prepared nanocomposites at absence (0 T) and present (0.2 T) magnetic field.

Sample	No external magnetic field			Under an external magnetic field (μoH=0.2 T)		
	Onset potential V (vs. SCE) -0T	Potential at current density 10 mA. cm^{-2} [V (vs. SCE)]	*η_{10} (mV)	Onset potential V (vs. SCE)	Potential at current density 10 mA. cm^{-2} [V (vs. SCE)]	*η_{10} (mV)
GO−5 %/NiAl-LDH	0.69	0.90	623	0.64	0.85	573
GO−3 %/NiAl-LDH	0.68	0.89	613	0.63	0.75	473
GO−1 %/NiAl-LDH	0.64	0.75	473	0.61	0.72	443
GO−0.5 %/NiAl-LDH	0.67	0.84	563	0.63	0.80	523
GO−0.3 %/NiAl-LDH	0.68	0.88	603	0.62	0.76	483
GO	0.73	0.95	673	0.76	1.02	743
NiAl-LDH	0.66	0.86	583	0.65	0.85	572

* Overpotential for current density 10 mA.cm^{-2}.

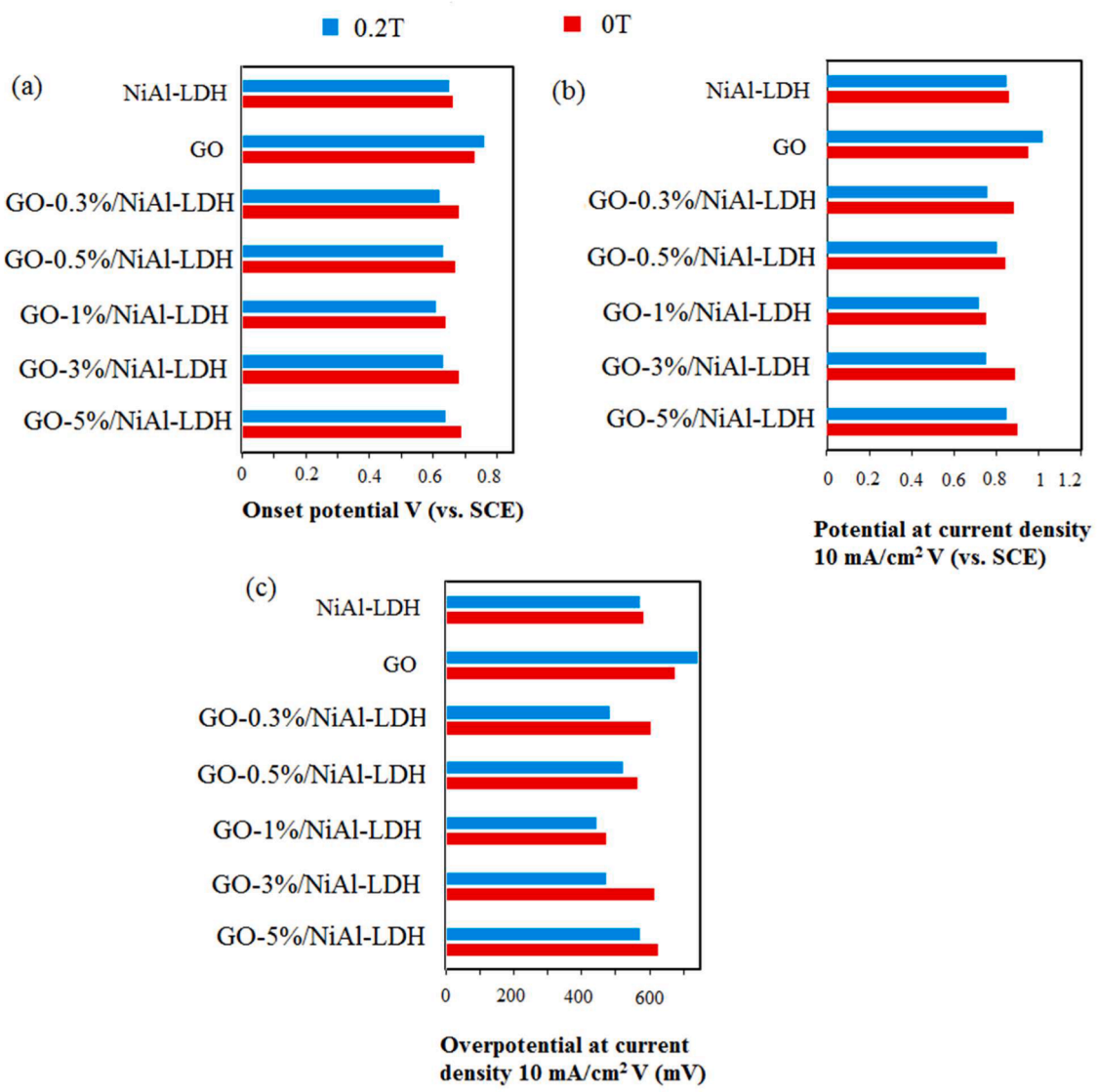

Fig. 7. Comparison of measured data of (a) onset potential, (b) potential at current density 10 mA.cm^{-2} V (vs. SCE), and (c) overpotential at current density 10 mA. cm^{-2} for prepared nanocomposites in the absence (0 T) and presence (0.2 T) of the magnetic field.

charge transfer resistance for GO-1 %/NiAl-LDH nanocomposites. To gain a deeper understanding of electron transfer kinetics under the influence of a magnetic field, we conducted electrochemical impedance spectroscopy (EIS), as shown in Fig. 9(b). The charge transfer values for GO-1 %/NiAl-LDH-0.2 T (10.9 Ω.cm^2) and GO-1 %/NiAl-LDH (12.1 Ω. cm^2) are notably lower than the charge transfer values reported for

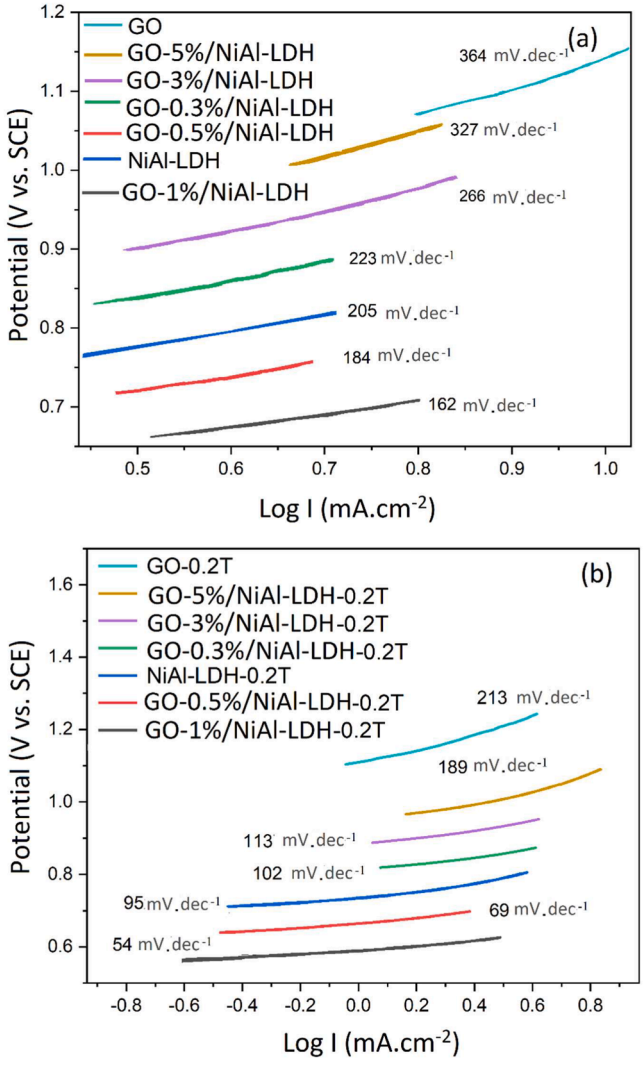

Fig. 8. Tafel slope of GO particles, NiAl-LDH particles and GO/NiAl-LDH nanocomposites with different GO contents drop casted on stainless steel substrate at (a) absence magnetic field and (b) present magnetic field ($\mu_o H$=*0.2 T*).

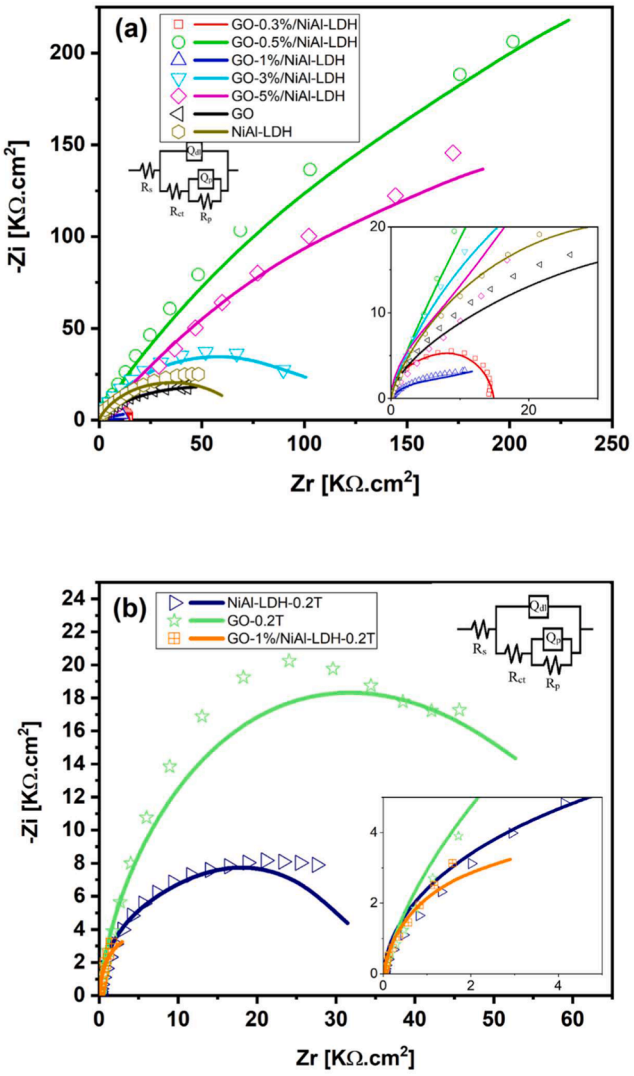

Fig. 9. EIS curves of (a) prepared nanocomposites in the absence of magnetic field (b) comparison of EIS curves of NiAl-LDH, GO, and GO-0.1 % /NiAl-LDH in the presence of the magnetic field ($\mu_o H$=*0.2 T)* (c) electrical equivalent circuit of prepared nanocomposites, NiAl-LDH, and GO.

Ni_3Fe-LDH/rGO/NF (16.3 Ω.cm^2) by Wang et al., [69] indicating that my materials exhibit a lower charge transfer rate. However, they are higher than the values observed for NiFe-LDH/rGO/NF (11.5 Ω.cm^2) and rGO/NF (23.1 Ω.cm^2), suggesting that my materials still have competitive charge transfer properties within this context[70,71].

The fitted data obtained from EIS curves are summarised in Table 2. The charge transfer resistance, denoted as R_{ct} and associated with high-frequency relaxation, exhibited a remarkably low value of 12.1 kΩ.cm^2 for GO-1 %/NiAl-LDH during the water oxidation reaction. This resistance was further reduced to 10.9 kΩ·cm^2 when a magnetic field was applied. Similarly, the resistance R_p, linked to intermediate frequency relaxation related to intermediate formation, decreased to 1.3 kΩ.cm^2 when a magnetic field was used. This observation suggests that the electrocatalytic activity of GO-1 %/NiAl-LDH electrodes is enhanced when subjected to an external magnetic field, surpassing what is typically observed with the effects of an external magnetic field in OER[41, 70].

The inherent role of a magnetic field in regulating electrocatalytic performance, specifically in the context of this research is discussed briefly and sumamrised here which, involves several key mechanisms influencing the water oxidation reactions (OER) including:

Table 2
Fitted data obtained from EIS curves.

Sample	R_s (Ω.cm^2)	Q_{dl} (μF)	R_{ct} (Ω.cm^2)	R_p (kΩ.cm^2)	Q_p (μF)	n
GO−0.5 %/NiAl-LDH	25.6	72.1	220.8	2.2	3.3	0.90
GO−1 %/NiAl-LDH	26.4	1.3 (mF)	12.1	1.3	4.7 (uF)	0.84
GO−1 %/NiAl-LDH −0.2 T	54.6	1.6 (mF)	10.9	2.5	6.5	0.86
GO−3 %/NiAl-LDH	26.4	125.8	79.8	1.2	4.4	0.79
GO−5 %/NiAl-LDH	31.8	21.4	744.1	1.2	4.3	0.79
GO	23.4	110.4	36.2	0.8	4.0	0.85
GO−0.2 T	10.5	710.1	23.9	0.8	1.4	0.91
NiAl-LDH	89.0	66.1	38.1	2.2	1.8	0.77
NiAl-LDH−0.2 T	17.9	48.1	10.7	5.3	4.8	0.84

3.6.1. *Magneto-hydrodynamic (MHD) effect*

The application of a magnetic field creates the Lorentz force ($f_L = j \times B$), where **j** represents the current density, and **B** is the magnetic

induction. This force drives the movement of electrolytes or convection, improving mass transport as well as the reduction of accumulated gas bubbles on the electrode surface. This reduction in bubble coverage enhances the availability of active sites for the OER and decreases the overpotential required for the reaction to occur.

3.6.2. Improvement in charge transfer

The magnetic field can enhance electron transfer rates across the electrode interface. In the case of the GO/NiAl-LDH nanocomposite studied, the presence of a magnetic field decreased the charge transfer resistance (Rct), as is evidenced by electrochemical impedance spectroscopy (EIS) results. This reduction in resistance facilitates better electron flow, thereby improving the overall catalytic efficiency of the electrocatalyst.

3.6.3. Reduction in overpotential

The application of a magnetic field significantly lowers the onset potential and overpotential during water oxidation. For example, the GO-1 %/NiAl-LDH nanocomposite exhibited a lower onset potential (0.61 V vs. SCE) and overpotential (443 mV) when a magnetic field was applied. This reduction is attributed to the combined effects of improved mass transport, better bubble management, and enhanced electron transfer.

3.6.4. Tafel slope reduction

The presence of a magnetic field also influences the reaction kinetics, as indicated by the reduction in the Tafel slope for the GO/NiAl-LDH nanocomposite under magnetic field conditions. This suggests a more favorable reaction pathway for OER, further enhancing the electrocatalytic performance.

In summary, the magnetic field plays a crucial role for tuning the electrocatalytic performance by enhancing mass transport, improving electron transfer, and reducing both overpotential and the Tafel slope. These effects ultimately lead to a more efficient and effective electrocatalytic process in water oxidation reactions.

3.7. Stability of GO/NiAl-LDH nanocomposites during water oxidation

Besides high OER activity, the durability of an electrocatalyst is another crucial issue for practical applications. Chronoamperometry test was performed to verify the stability of the GO-1 %/NiAl-LDH. The time-dependent behaviour of the GO-1 %/NiAl-LDH electrocatalyst in OER has been investigated in KOH 0.1 M under a constant potential of 0.95 V vs. SCE and is shown in Fig. 10(a). As it can be seen in the Fig. 10(a), during first 6 min, the current density increases at the beginning from 8.5 to 10.22 mA.cm^{-2} most likely due to the increased active surface area of the nanostructured electrode and diffusion of electrolyte into the electrode surface. However, after 1 h, the current density decreases from

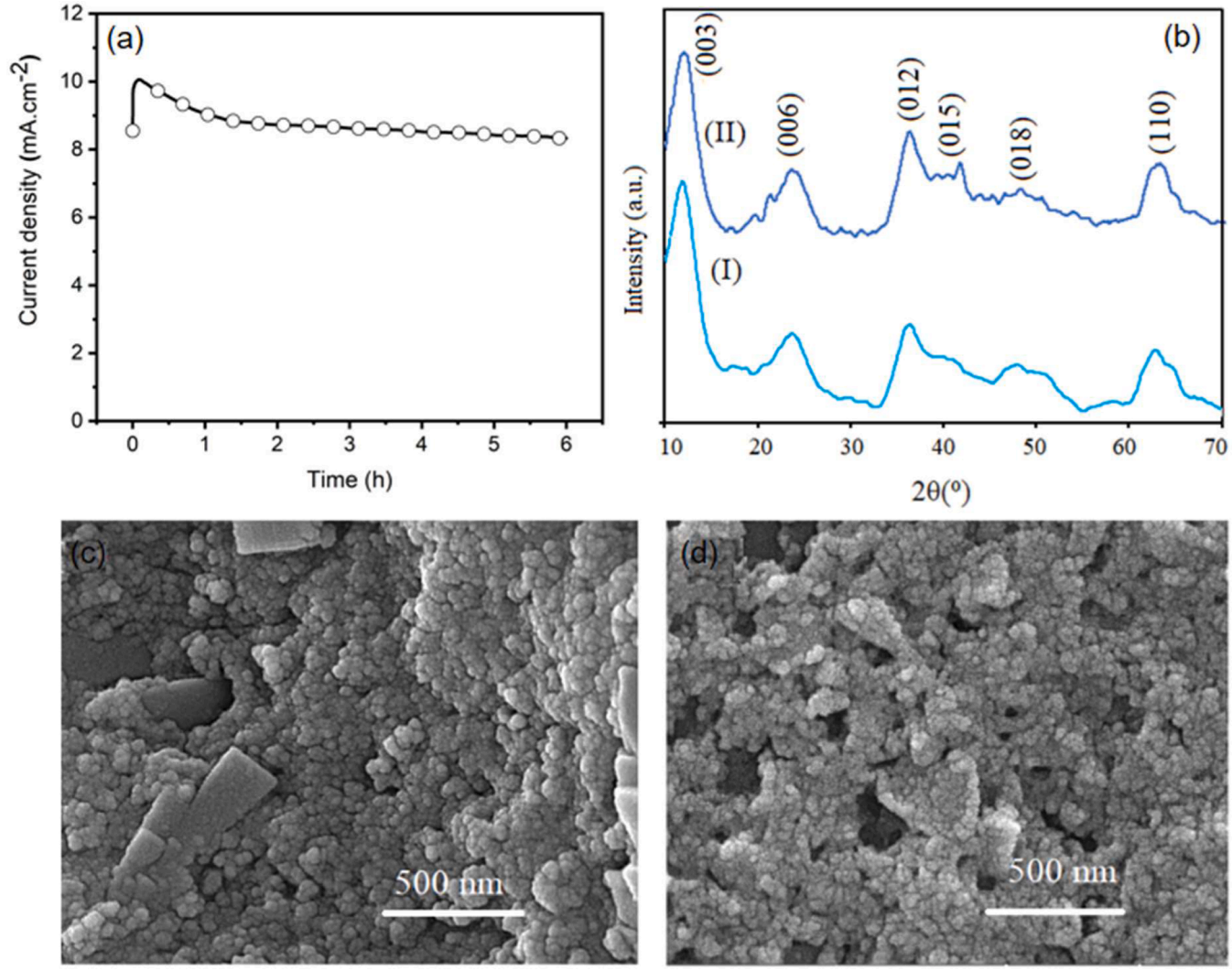

Fig. 10. (a) Time-dependent current density (chronoamperogram) curves for OER on the GO-1 %/NiAl-LDH, **(b)** XRD patterns of the GO-1 %/NiAl-LDH electrocatalyst before (pattern I) and after 6 h electrolysis (pattern II), and FE-SEM image of GO-1 %/NiAl-LDH, **(c)** after OER and **(d)** before 6 h OER.

8.25 mA.cm^{-2} which gives rise to an efficiency drop of 97 %. These findings confirm the excellent stability of the GO-1 %/NiAl-LDH. Moreover, for the structural stability study of the present electrocatalyst, we employed XRD of the electrocatalysts after 6 hrs of OER performance. The XRD pattern of the GO-1 %/NiAl-LDH examined after a long OER operation (6 h of electrolysis) shown in Fig. 10(b), pattern II was compared with that of as-prepared GO-1 %/NiAl-LDH, Fig. 10(a), pattern I. As can be seen both of XRD patterns of the GO-1 %/NiAl-LDH before and after water electrolysis is completely consistent with the pristine crystalline GO-1 %/NiAl-LDH phase (before electrolysis), suggesting no change in the LDH phase through OER catalysis. Besides, as shown at Fig. 10(c) and (d), after OER during 6 h, there are no change of the morphology of GO-1 %/NiAl-LDH. Thus, the GO-1 %/NiAl-LDH has sifficient OER activity and highly stable structure for water oxidation.

4. Conclusion

GO/NiAl-LDH nanocomposites were synthesized using the co-precipitation method. XRD, FT-IR, and FE-SEM analyses confirmed the successful hybridization of GO with NiAl-LDH, forming GO-x%/NiAl-LDH (x = 0.3, 0.5, 1, 3, and 5). The results of LSV, Tafel plots, and EIS curves demonstrate that the optimized GO/NiAl-LDH nanocomposite enhances the water oxidation reaction. The onset potential and overpotential at a current density of 10 mA.cm^{-2} were recorded at approximately 0.61 V (vs. SCE) and 443 mV, respectively, which are comparable to those of pure NiAl-LDH electrodes.This can be attributed to the increased charge transfer and high active sites at GO-1 %/NiAl-LDH. Under the influence of a magnetic field, the GO-1 %/NiAl-LDH nanocomposite shows enhanced water oxidation performance, attributed to the reduction in oxygen bubble formation on the electrode surface due to Lorentzian motion and an increase in electroactive sites. It was observed that the synthesized nanocomposite with a GO of about 0.01 g (GO-1 %/NiAl-LDH) acquires the lowest onset potential, about 0.61 V (vs. SCE) to start water oxidation under a magnetic field.

CRediT authorship contribution statement

Solmaz Komari-Alaei: Writing – original draft, Validation, Resources, Methodology, Investigation. **Amirali Farmani:** Writing – original draft, Resources, Methodology, Investigation, Data curation. **Sara Fazli-Shokouhi:** Writing – original draft, Validation, Investigation. **Naimeh-sadat Peighambardoust:** Writing – original draft, Validation, Resources, Methodology, Formal analysis, Data curation. **Farzad Nasirpouri:** Writing – review & editing, Validation, Supervision, Resources, Project administration, Methodology, Investigation, Funding acquisition, Formal analysis, Conceptualization. **Leila Jafari-Foruzin:** Writing – review & editing, Writing – original draft, Validation, Methodology, Investigation, Conceptualization.

Declaration of Competing Interest

The authors declare that they have no known competing financial interests or personal relationships that could have appeared to influence the work reported in this paper.

Acknowledgment

Iran Science Elites Federation is acknowledged for financial support of this research under the framework of the top 100 Iranian scientist award (FN) and postdoctoral award (LJF), 2021 numbered 400216 (1400–3–12).

Appendix A. Supporting information

Supplementary data associated with this article can be found in the online version at doi:10.1016/j.ijoes.2024.100841.

References

[1] Y. Huang, W. Zhou, W. Kong, L. Chen, X. Lu, H. Cai, Y. Yuan, L. Zhao, Y. Jiang, H. Li, Atomically interfacial engineering on molybdenum nitride quantum dots decorated N-doped graphene for high-rate and stable alkaline hydrogen production, Adv. Sci. 9 (36) (2022) 2204949, https://doi.org/10.1002/advs.202204949.

[2] Z. Wu, Q. Li, G. Xu, W. Jin, W. Xiao, Z. Li, T. Ma, S. Feng, L. Wang, Microwave phosphine-plasma-assisted ultrafast synthesis of halogen-doped Ru/RuP_2 with surface intermediate adsorption modulation for efficient alkaline hydrogen evolution reaction, Adv. Mater. 36 (13) (2024) 2311018, https://doi.org/10.1002/adma.202311018.

[3] P. Yang, F. Liu, X. Zang, L. Xin, W. Xiao, G. Xu, H. Li, Z. Li, T. Ma, J. Wang, Microwave quasi-solid state to construct strong metal-support interactions with interfacial electron-enriched Ru for anion exchange membrane electrolysis, Adv. Energy Mater. 14 (8) (2024) 2303384, https://doi.org/10.1002/aenm.202303384.

[4] Y.N. Zhou, W.L. Yu, H.J. Liu, R.Y. Fan, G.Q. Han, B. Dong, Y.M. Chai, Self-integration exactly constructing oxygen-modified MoNi alloys for efficient hydrogen evolution, EcoEnergy 1 (2) (2023) 425–436, https://doi.org/10.1002/ece2.19.

[5] Q. Li, X. Luan, Z. Xiao, W. Xiao, G. Xu, Z. Li, Z. Wu, L. Wang, Ultrafast microwave synthesis of Ru-doped MoP with abundant P vacancies as the electrocatalyst for hydrogen generation in a wide pH range, Inorg. Chem. 62 (24) (2023) 9687–9694, https://doi.org/10.1021/acs.inorgchem.3c01299.

[6] F. Musharavati, S. Khanmohammadi, Design and exergy based optimization of a clean energy system with fuel Cell/MED and hydrogen storage option, Int. J. Hydrog. Energy 47 (62) (2022) 26715–26727, https://doi.org/10.1016/j.ijhydene.2021.07.214.

[7] P. Sudalaimuthu, R. Sathyamurthy, The clean energy aspect of plastic waste—hydrogen gas production, CO_2 reforming, and plastic waste management coincide with catalytic pyrolysis—an extensive review, Environ. Sci. Pollut. Res. (2023) 1–26, https://doi.org/10.1007/s11356-023-26908-3.

[8] N. Zhang, Y. Chai, Lattice oxygen redox chemistry in solid-state electrocatalysts for water oxidation, Energy Environ. Sci. 14 (9) (2021) 4647–4671, https://doi.org/10.1039/D1EE01277K.

[9] Y. Song, W. Xie, M. Shao, X. Duan, Integrated electrocatalysts derived from metal organic frameworks for gas-involved reactions, Nano Mater. Sci. 5 (2) (2023) 161–176, https://doi.org/10.1016/j.nanoms.2022.01.003.

[10] J. Hu, D. Jiang, Z. Weng, Y. Pan, Z. Li, H. Du, Y. Yuan, A universal electrochemical activation enabling lattice oxygen activation in nickel-based catalyst for efficient water oxidation, Chem. Eng. J. 430 (2022) 132736, https://doi.org/10.1016/j.cej.2021.132736.

[11] S. Chen, S. Zhang, L. Guo, L. Pan, C. Shi, X. Zhang, Z.-F. Huang, G. Yang, J.-J. Zou, Reconstructed Ir-O-Mo species with strong Brønsted acidity for acidic water oxidation, Nat. Commun. 14 (1) (2023) 4127, https://doi.org/10.1038/s41467-023-39822-6.

[12] Y. Wang, Y. Jiang, Y. Zhao, X. Ge, Q. Lu, T. Zhang, D. Xie, M. Li, Y. Bu, Design strategies of perovskite nanofibers electrocatalysts for water splitting: A mini review, Chem. Eng. J. 451 (2023) 138710, https://doi.org/10.1016/j.cej.2022.138710.

[13] M.S.A. Sher Shah, G.Y. Jang, K. Zhang, J.H. Park, Transition metal carbide-based nanostructures for electrochemical hydrogen and oxygen evolution reactions, EcoEnergy 1 (2) (2023) 344–374, https://doi.org/10.1002/ece2.18.

[14] Y. Huang, Y. Sun, X. Zheng, T. Aoki, B. Pattengale, J. Huang, X. He, W. Bian, S. Younan, N. Williams, Atomically engineering activation sites onto metallic 1T-MoS_2 catalysts for enhanced electrochemical hydrogen evolution, Nat. Commun. 10 (1) (2019) 982, https://doi.org/10.1038/s41467-019-08877-9.

[15] K. Du, L. Zhang, J. Shan, J. Guo, J. Mao, C.-C. Yang, C.-H. Wang, Z. Hu, T. Ling, Interface engineering breaks both stability and activity limits of RuO_2 for sustainable water oxidation, Nat. Commun. 13 (1) (2022) 5448, https://doi.org/10.1038/s41467-022-33150-x.

[16] I. Evazzade, A. Zagalskaya, V. Alexandrov, On the role of interfacial water dynamics for electrochemical stability of RuO_2 and IrO_2, ChemCatChem 14 (21) (2022) e202200932, https://doi.org/10.1002/cctc.202200932.

[17] R. Samanta, P. Panda, R. Mishra, S. Barman, IrO_2-Modified RuO_2 nanowires/nitrogen-doped carbon composite for effective overall water splitting in all pH, Energy Fuels 36 (2) (2022) 1015–1026, https://doi.org/10.1021/acs.energyfuels.1c04082.

[18] X. Lu, S. Lalwani, L. Yuan, M.A. Abdelsalam, F. AlMarzooqi, T. Zhang, Accelerated bubble departure and reduced overpotential with nanoengineered porous bifunctional Ni_5P_4 electrocatalyst for PV-driven water splitting, Int. J. Hydrog. Energy 47 (86) (2022) 36504–36516, https://doi.org/10.1016/j.ijhydene.2022.08.189.

[19] G. Liu, Y. Xu, T. Yang, L. Jiang, Recent advances in electrocatalysts for seawater splitting, Nano Mater. Sci. 5 (1) (2023) 101–116, https://doi.org/10.1016/j.nanoms.2020.12.003.

[20] H. Wang, P. Yang, X. Sun, W. Xiao, X. Wang, M. Tian, G. Xu, Z. Li, Y. Zhang, F. Liu, Co-Ru alloy nanoparticles decorated onto two-dimensional nitrogen doped carbon nanosheets towards hydrogen/oxygen evolution reaction and oxygen reduction reaction, J. Energy Chem. 87 (2023) 286–294, https://doi.org/10.1016/j.jechem.2023.08.039.

[21] Y. Shi, B. Zhang, Recent advances in transition metal phosphide nanomaterials: synthesis and applications in hydrogen evolution reaction, Chem. Soc. Rev. 45 (6) (2016) 1529–1541, https://doi.org/10.1039/C5CS00434A.

[22] E. Fabbri, A. Habereder, K. Waltar, R. Kötz, T.J. Schmidt, Developments and perspectives of oxide-based catalysts for the oxygen evolution reaction, Catal. Sci. Technol. 4 (11) (2014) 3800–3821, https://doi.org/10.1039/C4CY00669K.
[23] H. Kim, H. Park, M. Kang, J.Y. Park, Plasmonic hot carrier-driven photoelectrochemical water splitting on antenna–reactor Pt/Ag/TiO2 Schottky nanodiodes, J. Chem. Phys. 157 (8) (2022), https://doi.org/10.1063/5.0097713.
[24] Z.U. Khan, M. Alsaiari, M.A. Ahmed, N. Muhammad, M. Tariq, A. Rahim, A. Niaz, Catalysts for electrochemical water splitting for hydrogen production, Mater. Hydrog. Prod., Convers., Storage (2023) 225–247, https://doi.org/10.1002/9781119829584.ch8.
[25] C. Kuai, Z. Xu, C. Xi, A. Hu, Z. Yang, Y. Zhang, C.-J. Sun, L. Li, D. Sokaras, C. Dong, Phase segregation reversibility in mixed-metal hydroxide water oxidation catalysts, Nat. Catal. 3 (9) (2020) 743–753, https://doi.org/10.1038/s41929-020-0496-z.
[26] R. Gao, J. Zhu, D. Yan, Transition metal-based layered double hydroxides for photo (electro) chemical water splitting: a mini review, Nanoscale 13 (32) (2021) 13593–13603, https://doi.org/10.1039/D1NR03409J.
[27] P.K. Ray, R. Mohanty, K. Parida, Recent advancements of NiCo LDH and graphene based nanohybrids for supercapacitor application, J. Energy Storage 72 (2023) 108335, https://doi.org/10.1016/j.est.2023.108335.
[28] P.M. Bodhankar, P.B. Sarawade, G. Singh, A. Vinu, D.S. Dhawale, Recent advances in highly active nanostructured NiFe LDH catalyst for electrochemical water splitting, J. Mater. Chem. A 9 (6) (2021) 3180–3208, https://doi.org/10.1039/D0TA10712C.
[29] T. Tang, X. Li, Z. Feng, Y. Liu, A needle-like cobalt-based bifunctional catalyst supported on carbon materials for effective overall water splitting, Nanotechnology 33 (6) (2021) 065704, https://doi.org/10.1088/1361-6528/ac328d.
[30] T. Wang, M. Xu, F. Li, Y. Li, W. Chen, Multimetal-based nitrogen doped carbon nanotubes bifunctional electrocatalysts for triiodide reduction and water-splitting synthesized from polyoxometalate-intercalated layered double hydroxide pyrolysis strategy, Appl. Catal. B: Environ. 280 (2021) 119421, https://doi.org/10.1016/j.apcatb.2020.119421.
[31] M. Gong, Y. Li, H. Wang, Y. Liang, J.Z. Wu, J. Zhou, J. Wang, T. Regier, F. Wei, H. Dai, An advanced Ni–Fe layered double hydroxide electrocatalyst for water oxidation, J. Am. Chem. Soc. 135 (23) (2013) 8452–8455, https://doi.org/10.1021/ja4027715.
[32] P. Yin, G. Wu, X. Wang, S. Liu, F. Zhou, L. Dai, X. Wang, B. Yang, Z.-Q. Yu, NiCo-LDH nanosheets strongly coupled with GO-CNTs as a hybrid electrocatalyst for oxygen evolution reaction, Nano Res. 14 (12) (2021) 4783–4788, https://doi.org/10.1007/s12274-021-3424-x.
[33] J. Xie, C. Li, J. Niu, S. Zhang, X. Ou, P. Feng, H. Garcia, Porous NiFe-LDH grown on graphene oxide towards highly efficient OER electrocatalysis, Mater. Lett. 290 (2021) 129517, https://doi.org/10.1016/j.matlet.2021.129517.
[34] X. Han, N. Suo, C. Chen, Z. Lin, Z. Dou, X. He, L. Cui, Graphene oxide guiding the constructing of nickel-iron layered double hydroxides arrays as a desirable bifunctional electrocatalyst for HER and OER, Int. J. Hydrog. Energy 44 (57) (2019) 29876–29888, https://doi.org/10.1016/j.ijhydene.2019.09.116.
[35] D.-c Xia, L. Zhou, S. Qiao, Y. Zhang, D. Tang, J. Liu, H. Huang, Y. Liu, Z. Kang, Graphene/Ni–Fe layered double-hydroxide composite as highly active electrocatalyst for water oxidation, Mater. Res. Bull. 74 (2016) 441–446, https://doi.org/10.1016/j.materresbull.2015.11.007.
[36] W. Ma, R. Ma, C. Wang, J. Liang, X. Liu, K. Zhou, T. Sasaki, A superlattice of alternately stacked Ni–Fe hydroxide nanosheets and graphene for efficient splitting of water, ACS Nano 9 (2) (2015) 1977–1984, https://doi.org/10.1021/nn5069836.
[37] J. Chang, Z. Hu, J. Li, D. Wu, Z. Lian, F. Xu, K. Jiang, Z. Gao, Ultrathin NiAl layered double hydroxide-reduced graphene oxide composite nanosheets array with high battery performances for hybrid supercapacitor and hybrid battery, Appl. Surf. Sci. 538 (2021) 148106, https://doi.org/10.1016/j.apsusc.2020.148106.
[38] Y. Han, N. Liu, N. Wang, Z. He, Q. Liu, Assembly of Ni–Al layered double hydroxide and oxide graphene quantum dots for supercapacitors, J. Mater. Res. 33 (24) (2018) 4215–4223, https://doi.org/10.1557/jmr.2018.424.
[39] X. Xu, S. Shi, Y. Tang, G. Wang, M. Zhou, G. Zhao, X. Zhou, S. Lin, F. Meng, Growth of NiAl-layered double hydroxide on graphene toward excellent anticorrosive microwave absorption application, Adv. Sci. 8 (5) (2021) 2002658, https://doi.org/10.1002/advs.202002658.
[40] F.A. Garcés-Pineda, M. Blasco-Ahicart, D. Nieto-Castro, N. López, J.R. Galán-Mascarós, Direct magnetic enhancement of electrocatalytic water oxidation in alkaline media, Nature, Energy 4 (6) (2019) 519–525, https://doi.org/10.1038/s41560-019-0404-4.
[41] A.A. Farmani, F. Nasirpouri, Boosting hydrogen and oxygen evolution reactions on electrodeposited nickel electrodes via simultaneous mesoporosity, magnetohydrodynamics and high gradient magnetic force, J. Mater. Chem. A 8 (46) (2020) 24782–24799, https://doi.org/10.1039/D0TA06906J.
[42] S. Fazli-Shokouhi, F. Nasirpouri, M. Khatamian, Epoxy-matrix polyaniline/p-phenylenediamine-functionalised graphene oxide coatings with dual anti-corrosion and anti-fouling performance, RSC Adv. 11 (19) (2021) 11627–11641, https://doi.org/10.1039/D0RA10665H.
[43] S. Fazli-Shokouhi, F. Nasirpouri, M. Khatamian, Polyaniline-modified graphene oxide nanocomposites in epoxy coatings for enhancing the anticorrosion and antifouling properties, J. Coat. Technol. Res. 16 (2019) 983–997, https://doi.org/10.1007/s11998-018-00173-3.
[44] L. Li, K.S. Hui, K.N. Hui, Q. Xia, J. Fu, Y.-R. Cho, Facile synthesis of NiAl layered double hydroxide nanoplates for high-performance asymmetric supercapacitor, J. Alloy. Compd. 721 (2017) 803–812, https://doi.org/10.1016/j.jallcom.2017.06.062.
[45] R. Siburian, H. Sihotang, S.L. Raja, M. Supeno, C. Simanjuntak, New route to synthesize of graphene nano sheets, Orient. J. Chem. 34 (1) (2018) 182, https://doi.org/10.13005/ojc/340120.
[46] X. Liu, X. Ge, M. Liu, K. Zhou, Q. Zhu, D. Chen, C. Liu, C. Wang, X. Liu, G. Tang, Facile fabrication of NiAl-LDH and its application in TPU nanocomposites targets for reducing fire hazards, Plast., Rubber Compos. 50 (6) (2021) 285–298, https://doi.org/10.1080/14658011.2021.1890515.
[47] X. Lei, B. Wang, J. Liu, Z. Ye, Z. Chang, M. Jiang, X. Sun, Three-dimensional NiAl-mixed metal oxide film: preparation and capacitive deionization performances, RSC Adv. 4 (78) (2014) 41642–41648, https://doi.org/10.1039/C4RA08415B.
[48] C. Nethravathi, T. Nisha, N. Ravishankar, C. Shivakumara, M. Rajamathi, Graphene–nanocrystalline metal sulphide composites produced by a one-pot reaction starting from graphite oxide, Carbon 47 (8) (2009) 2054–2059, https://doi.org/10.1016/j.carbon.2009.03.055.
[49] D. Tang, J. Liu, X. Wu, R. Liu, X. Han, Y. Han, H. Huang, Y. Liu, Z. Kang, Carbon quantum dot/NiFe layered double-hydroxide composite as a highly efficient electrocatalyst for water oxidation, ACS Appl. Mater. Interfaces 6 (10) (2014) 7918–7925, https://doi.org/10.1021/am501256x.
[50] S.K. Sen, U.C. Barman, M. Manir, P. Mondal, S. Dutta, M. Paul, M. Chowdhury, M. Hakim, X-ray peak profile analysis of pure and Dy-doped α-MoO_3 nanobelts using Debye-Scherrer, Williamson-Hall and Halder-Wagner methods, Adv. Nat. Sci.: Nanosci. Nanotechnol. 11 (2) (2020) 025004, https://doi.org/10.1088/2043-6254/ab8732.
[51] M. Li, W. Yin, X. Han, X. Chang, Hierarchical nanocomposites of polyaniline scales coated on graphene oxide sheets for enhanced supercapacitors, J. Solid State Electrochem. 20 (2016) 1941–1948, https://doi.org/10.1007/s10008-016-3202-y.
[52] F. Thema, M. Moloto, E. Dikio, N. Nyangiwe, L. Kotsedi, M. Maaza, M. Khenfouch, Synthesis and characterization of graphene thin films by chemical reduction of exfoliated and intercalated graphite oxide, J. Chem. 2013 (2013), https://doi.org/10.1155/2013/150536.
[53] J. Sun, H. Bi, Pickering emulsion fabrication and enhanced supercapacity of graphene oxide-covered polyaniline nanoparticles, Mater. Lett. 81 (2012) 48–51, https://doi.org/10.1016/j.matlet.2012.04.078.
[54] C.Y. Abasi, P.N. Diagboya, E.D. Dikio, Layered double hydroxide of cobalt-zinc-aluminium intercalated with carbonate ion: preparation and Pb (II) ion removal capacity, Int. J. Environ. Stud. 76 (2) (2019) 251–265, https://doi.org/10.1080/00207233.2018.1517935.
[55] D. Chu, F. Li, X. Song, H. Ma, L. Tan, H. Pang, X. Wang, D. Guo, B. Xiao, A novel dual-tasking hollow cube $NiFe_2O_4$-NiCo-LDH@ rGO hierarchical material for high preformance supercapacitor and glucose sensor, J. Colloid Interface Sci. 568 (2020) 130–138, https://doi.org/10.1016/j.jcis.2020.02.012.
[56] P. Huang, C. Cao, Y. Sun, S. Yang, F. Wei, W. Song, One-pot synthesis of sandwich-like reduced graphene oxide@ CoNiAl layered double hydroxide with excellent pseudocapacitive properties, J. Mater. Chem. A 3 (20) (2015) 10858–10863, https://doi.org/10.1039/C5TA02427G.
[57] L. Dou, H. Zhang, Facile assembly of nanosheet array-like CuMgAl-layered double hydroxide/rGO nanohybrids for highly efficient reduction of 4-nitrophenol, J. Mater. Chem. A 4 (48) (2016) 18990–19002, https://doi.org/10.1039/C6TA08313G.
[58] X. Xiang, L. Bai, F. Li, Formation and catalytic performance of supported ni nanoparticles via self-reduction of hybrid NiAl-LDH/C composites, AIChE J. 56 (11) (2010) 2934–2945, https://doi.org/10.1002/aic.12189.
[59] Z. Bian, H. Huang, Y. Ma, F. Guo, Y. Shang, Y. Zhang, J. Xu, NiAl-Layer double hydroxide loading on MXenes nanosheets with boehmite-assisted for improved electrochemical performance, Ionics 29 (6) (2023) 2365–2376, https://doi.org/10.1007/s11581-023-04987-z.
[60] S.P. Lonkar, J.M. Raquez, P. Dubois, One-Pot microwave-assisted synthesis of graphene/layered double hydroxide (LDH) nanohybrids, Nanomicro Lett. 7 (2015) 332–340, https://doi.org/10.1007/s40820-015-0047-3.
[61] W. Zhao, T. Liu, N. Wu, B. Zhou, Y. Yan, Y. Ye, J. Gong, S. Yang, Bimetallic electron-induced phase transformation of CoNi LDH-GO for high oxygen evolution and supercapacitor performance, Sci. China Mater. 66 (2) (2023) 577–586, https://doi.org/10.1007/s40843-022-2170-6.
[62] L. Feng, Y. Du, J. Huang, L. Cao, L. Feng, Y. Feng, Q. Liu, D. Yang, K. Kajiyoshi, Nanoporous NiAl-LDH nanosheet arrays with optimized Ni active sites for efficient electrocatalytic alkaline water splitting, Sustain. Energy Fuels 4 (6) (2020) 2850–2858, https://doi.org/10.1039/D0SE00050G.
[63] Z. Yang, S. Ji, W. Gao, C. Zhang, L. Ren, W.W. Tjiu, Z. Zhang, J. Pan, T. Liu, Magnetic nanomaterial derived from graphene oxide/layered double hydroxide hybrid for efficient removal of methyl orange from aqueous solution, J. Colloid Interface Sci. 408 (2013) 25–32, https://doi.org/10.1016/j.jcis.2013.07.011.
[64] S. Nayak, K. Parida, Superactive NiFe-LDH/graphene nanocomposites as competent catalysts for water splitting reactions, Inorg. Chem. Front. 7 (20) (2020) 3805–3836, https://doi.org/10.1039/D0QI00700E.
[65] T. Shinagawa, A.T. Garcia-Esparza, K. Takanabe, Insight on Tafel slopes from a microkinetic analysis of aqueous electrocatalysis for energy conversion, Sci. Rep. 5 (1) (2015) 13801, https://doi.org/10.1038/srep13801.
[66] A.C. Lazanas, M.I. Prodromidis, Electrochemical impedance spectroscopy— a tutorial, ACS Meas. Sci. Au 3 (3) (2023) 162–193, https://doi.org/10.1021/acsmeasuresciau.2c00070.
[67] F.S. Gill, D. Uniyal, B. Prasad, S. Saluja, A. Mishra, R.K. Bachheti, S. Juyal, Investigation of increased electrical conductivity by rGO in rGO/PVDF/PMMA/PTFE nanocomposites, J. Mol. Struct. 1267 (2022) 133541, https://doi.org/10.1016/j.molstruc.2022.133541.
[68] W. Chen, B. Wu, Y. Wang, W. Zhou, Y. Li, T. Liu, C. Xie, L. Xu, S. Du, M. Song, Deciphering the alternating synergy between interlayer Pt single-atom and NiFe

layered double hydroxide for overall water splitting, Energy Environ. Sci. 14 (12) (2021) 6428–6440, https://doi.org/10.1039/D1EE01395E.
[69] K. Wang, J. Guo, H. Zhang, Synergistic effect of nanosheet-array-like NiFe-LDH and reduced graphene oxide modified Ni foam for greatly enhanced oxygen evolution reaction and hydrogen evolution reaction, Mater. Adv. 3 (17) (2022) 6887–6896, https://doi.org/10.1039/D2MA00370H.
[70] D. Xu, Y. Rui, Y. Li, Q. Zhang, H. Wang, Zn-Co layered double hydroxide modified hematite photoanode for enhanced photoelectrochemical water splitting, Appl. Surf. Sci. 358 (2015) 436–442, https://doi.org/10.1016/j.apsusc.2015.08.160.
[71] F. Nasirpouri, A. Farmani, S. Safarpour, Ultrasonic-assisted pulse electrodeposition process for producing nanocrystalline nickel films and their corrosion behavior: Competition between mass transport and nucleation, Surf. Coat. Technol. (2024) 130996, https://doi.org/10.1016/j.surfcoat.2024.130996.